CHAPTER 2

Transport properties of nanoscopic solids as probed by spectroscopic techniques

Dejan M. Djokić[1], Novica Paunović[1], Bojan Stojadinović[1], Dimitrije Stepanenko[1], Saša Lazović[2], Zorana Dohčević-Mitrović[1]

[1]Nanostructured Matter Laboratory, Institute of Physics Belgrade, University of Belgrade, Belgrade, Serbia; [2]Biomimetics Laboratory, Institute of Physics Belgrade, University of Belgrade, Belgrade, Serbia

Chapter Outline

1. Introduction

Nanoscale world is at the border between the quantum realm at the smaller dimensions and the classical one at larger. At the quantum side of this divide, systems under consideration consist of few particles and the properties of the sample often do not average into well-behaved quantities with deviations from the mean value much smaller than the mean value itself. So standard assumptions of both the classical physics and the standard statistics can break down within the nanoscale domain. This occurrence impacts the methods for probing the transport at the nanoscale.

Fundamentals and Properties of Multifunctional Nanomaterials. https://doi.org/10.1016/B978-0-12-822352-9.00009-2
Copyright © 2021 Elsevier Inc. All rights reserved.

Noncontact measurements of transport can offer distinct advantages. Macroscopic contacts necessary for the standard transport measurements often disturb the system since they are immensely larger than it. The structure of the contacts needs to impact the system as little as possible, requiring cooling to very low temperatures. Thermal noise introduced by contacts is hard to distinguish from the quantum noise that is an interesting property of the probed system.

Experiment is always performed on an object composed of nonidentical units and averaging of the properties does not automatically occur within the measurement apparatus. Moreover, the most interesting properties are often encoded into distribution of the results of measurements, and not exclusively in their mean values. Quantum side of the breakdown is somewhat different. The quantum transport theory deals with universality of the transport. In the quantum limit, as most transparently seen in the Landauer formula for conductivity, the whole variety of the transport behavior boils down to the number and transmitivities of transport channels. The variety of quantum behavior in transport appears due to macroscopic quantum phenomena or lies hidden in the variability of nominally identical nanoscale systems.

To probe the rich variety of transport phenomena at the nanoscale, it is preferable to look at the properties of conducting quasiparticles than to look at the integral characteristics of a collection of them. Quasiparticles are most easily accessed through spectroscopic techniques, like Raman spectroscopy, electron spin resonance (ESR), and infrared reflection (IRR) spectroscopy. Resonant nature of excitations and response detection in spectroscopy offer us a way to discriminate between constituents of the nanoscale system and look exclusively at the processes that are in resonance with the appropriate driving. Therefore the noncontact spectroscopic measurements give us an opportunity to see the nanoscale world in more detail.

This chapter is partitioned in three sections which are organized as follows. In the first section, we provide a short introduction to the Raman scattering technique followed with a review on an indirect finding of the two different variable range hopping (VRH) transport mechanisms based on the analysis of the temperature dependent electronic Raman background of nanocrystalline $BiFeO_3$ [1]. The subsequent section tackles a summary on how both particle size decreased and Nd doping influence the Plasmon−phonon interaction and optical conductivity in CeO_{2-y} nanocrystals investigated by IRR spectroscopy [2]. Finally, in the third section, the main aspects of conduction ESR have been briefly introduced in which terms the temperature evolution and character of transport properties of single-walled carbon nanotubes have been elaborated [3].

2. Raman scattering

2.1 Short introduction to Raman scattering technique

In solid state spectroscopy, the inelastic scattering of photons by lattice vibrations (LVs) is known as Raman effect. The photon energy can be lost or gained in such processes, which

is accomplished by the phonon creation or annihilation, and termed in literature as Stokes or anti-Stokes Raman excitation, respectively. Brillouin Raman scattering (RS), however, stands for a particular case of RS that concerns the scattering by acoustic phonons of very low frequencies, unlike common Raman which involves optical phonons. The theory of Raman spectroscopy can be found elsewhere. Nevertheless, for a rather comprehensive elaboration the reader is further referred to seminal Mitra's work [4], some of which fragments we will rely on in what follows.

Following the first principles of electromagnetism, the incident electromagnetic field of the photons is coupled with the phonons via dipole moments that are induced by the phonon field. The electronic 3×3 polarizability tensor α_{mn} is modulated by the variation of the lattice due to the normal vibration of frequency ω_p and can be expanded in terms of the time dependent atomic displacement components $u_p = u_p(0)e^{i\omega_p t}$ as

$$\alpha_{mn} = \alpha_{mn}^{(0)} + \sum_p \alpha_{mn,p}^{(1)} u_p + \frac{1}{2}\sum_p \sum_q \alpha_{mn,pq}^{(2)} u_p u_q + \ldots \tag{2.1}$$

where

$$\alpha_{mn,p}^{(1)} = \left(\frac{\partial \alpha_{mn}}{\partial u_p}\right)_{u_p=0}, \; \alpha_{mn,pq}^{(2)} = \left(\frac{\partial^2 \alpha_{mn}}{\partial u_p \partial u_q}\right)_{u_p=0,\, u_q=0} \ldots \tag{2.2}$$

If $\overrightarrow{E}$ denotes the electric field of incident electromagnetic radiation with frequency ω,

$$\overrightarrow{E} = \overrightarrow{E}(0)e^{i\omega t}, \tag{2.3}$$

then the induced dipole moment can be written as

$$\overrightarrow{M} = \widehat{\alpha}\overrightarrow{E}, \tag{2.4}$$

which ultimately yields induced dipole moment along p mode

$$\overrightarrow{M}_p = \widehat{\alpha}^{(0)}\overrightarrow{E}_0 e^{i\omega t} + \widehat{\alpha}^{(1)}\overrightarrow{E}_0 e^{i\left(\omega \pm \omega_p\right)t} u_p(0) + \widehat{\alpha}^{(2)}\overrightarrow{E}_0 e^{i\left(\omega \pm 2\omega_p\right)t} u_p^2(0) + \ldots \tag{2.5}$$

First term in Eq. (2.5) represents nothing but elastic Raleigh scattering process. The energy of the electromagnetic radiation remains unchanged in this case. The derivative of the electronic polarizability in the second term in Eq. (2.5) gives rise to the first-order RS processes when incident photon $\left(\hbar\overrightarrow{k}_1, \hbar\omega_1\right)$ is absorbed or created to create or destroy a phonon $\left(\hbar\overrightarrow{k}, \hbar\omega\right)$. The final photon, with both different wave vector and frequency $\left(\hbar\overrightarrow{k}_2, \hbar\omega_2\right)$ from the incident one, gets emitted in such a way that the energy and the momentum are totally conserved. Reduced Planck's constant is denoted as $\hbar$.

In doped semiconductors and disordered metals, spectral recoil of light in RS consistently comprises a number of distinctive peaks generated by optically active phonons, as well as, an extended frequency continuum which is in direct relationship with electronic response [6]. This continuous spectral background originates from low-energy electronic excitations, which reflects the charge carrier scattering rate, and is familiarly known in literature as the Raman electronic background [1,7–11]. Falkovsky [7] was first to provide a theoretical foundation for the spectral profiles of Raman electronic background in "dirty" metals. The effects of electronic excitations in Raman are usually observed at low-energy scales and are attributed to scattering by phonons or impurities involving finite momentum transfers ($k \neq 0$) as a result of the finite penetration depth of light in materials. Later on, Zawadowski and Cardona [8] proposed a Feynman diagrammatic approach to estimating the Kubo spectral response function within the scope of ladder approximation [12] at $q \approx 0$. Most importantly, these authors were first to recognize an intimately related link between the nonresonant electronic excitations seen in Raman with the carrier transport.

As with nonresonant RS electronic response, the related Feynman diagrams (see Fig. 2.1) are composed of wavy lines denoting photon propagators. Their initial and final (momentum, energy) are respectively $\left(\hbar\vec{k}_1, \hbar\omega_1\right)$ and $\left(\hbar\vec{k}_2, \hbar\omega_2\right)$. An electron-hole pair of (momentum: $\vec{k} = \vec{k}_1 - \vec{k}_2$, energy: $\omega = \omega_1 - \omega_2$), scattered by phonons and/or impurities, become generated by the incoming photon propagator. Phonon propagator, given in dashed line (Fig. 2.1), can be excited by the electron/hole inside a pair and is further captured by its counterpart (hole/electron), as is enforced by the ladder approximation. At last, upon summing up all the dominating ladder-like diagrams, Raman differential cross section due to the purely electronic response [9,11], reads as

$$\frac{\mathrm{d}^2\sigma}{\mathrm{d}\omega\mathrm{d}\Omega} \propto \frac{1}{1-\exp(-\hbar\omega/k_BT)} \times \frac{\omega\tau}{1+(\omega\tau)^2}. \tag{2.6}$$

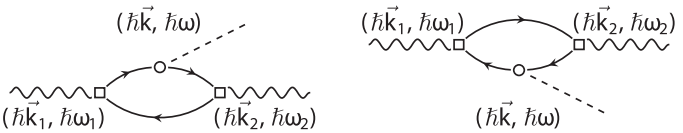

Figure 2.1

Raman scattering of light (*wavy lines*) due to phonons (*dashed lines*). Electron-hole formations (*solid lines*) represented via loops in the Feynman diagrams of third order (first order Raman scattering). Processes involving electron and hole contributions are given in left and right diagrams, respectively. Vertex □ represents electron-photon interaction, while vertex represents electron-phonon interaction as is given in Ref. [5]. *The drawing is adapted from D.M. Djokić, B. Stojadinović, D. Stepanenko, Z. Dohčević-Mitrović, Probing charge carrier transport regimes in $BiFeO_3$ nanoparticles by Raman spectroscopy, Scr. Mater. 181 (2020) 6–9. https://doi.org/10.1016/j.scriptamat.2020.02.008.*

At a particular value of the effective scattering rate, $1/\tau$, the proportionality factor in Eq. (2.6) is a function of different variables depending on the type of the experimental setup [10]. The temperature-dependent Bose-Einstein factor and expression resembling Drude function are respectively given as the second and third term in the product of Eq. (2.6), while $1/\tau$ involves two terms in the sum as follows

$$1/\tau = 1/\tau_0 + Dq^2. \tag{2.7}$$

$1/\tau_0$ stands for the charge carrier scattering rate due to phonons/impurities in $q \to 0$ limit, which is concerned with nothing but bulk channels. The second term (Dq^2), however, gives rise to the effects of processes nonconserving momenta, very often pronounced in nanocrystals [1]. It is safe to neglect the bulk term ($1/\tau_0$) if there is no experimental evidence for the electronic Raman background in the case of bulk materials. D is the diffusion constant which is, based on the Einstein relation, related to electric conductivity σ in the following manner

$$D = \sigma/\left(g(\varepsilon_F)e^2\right), \tag{2.8}$$

where $e = 1.6 \times 10^{-19}$ C. The average value of the electronic density states close to the Fermi level [9] is denoted with $g(\varepsilon_F)$.

2.2 Multiferroic $BiFeO_3$ nanoparticles

Crystalline bismuth ferrite stands for a multiferroic material increasingly attracting the attention among the researchers and is also one of few materials to provide both ferroelectric ($T_C \approx 1100$ K) and antiferromagnetic ($T_N \approx 643$ K) properties at room temperature [13] and even higher. It is important to know that $BiFeO_3$ has proven undemanding to obtain in ambient conditions. $BiFeO_3$ is classed as rhombohedrally distorted ABO_3 perovskite structure (space group $R3c$) with lattice parameter $a_{rh} = 3.965$ Å, a rhombohedral angle α_{rh} of 89.30−89.48°, and ferroelectric polarization along $[111]_{pseudocubic}$ direction at room temperature [14]. Primitive unit cell consists of two unit formulas and contains 10 atoms. This structure can be represented as two distorted perovskite unit cells, connected along the main pseudocubic diagonal [111] to form a rhombohedral unit cell, as is given in Fig. 2.2A. Bi^{3+} ions are situated at A lattice sites and are surrounded by 12 oxygen atoms. On the other hand side, Fe^{3+} ions are located at B lattice sites, and they are surrounded by six oxygen atoms with which it forms a FeO_6 octahedron. In this configuration, Bi^{3+} and Fe^{3+} ions are shifted along [111] direction, and two oxygen octahedrons are rotated around [111] direction in the opposite directions by 14° that can be seen from the position of the green octahedrons in Fig. 2.2B. This means that the Fe-O-Fe angle deviates from 180° to amount nearly 154−156° [16,17]. The unit cell can also be described in a hexagonal frame of reference, where the hexagonal

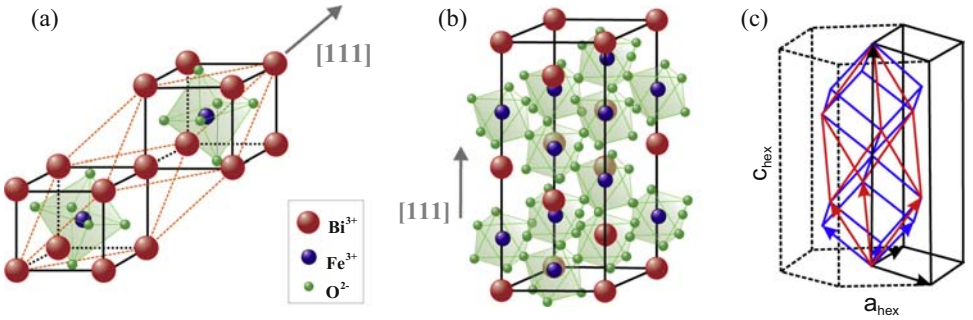

Figure 2.2

Schematic representation of (A) rhombohedral structure framed by orange dashed lines, (B) hexagonal perovskite structure of $BiFeO_3$ with [111] ferroelectric polarization direction given in gray arrow, and (C) hexagonal cell (black), rhombohedral (red), and pseudocubic (blue) unit cell with corresponding unit vectors drawn in *arrows*. *The figure is to a rather large extent reworked from J.-G. Park, M.D. Le, J. Jeong, S. Lee, Structure and spin dynamics of multiferroic $BiFeO_3$, J. Phys. Condens. Mat. 26 (2014) 433202. https://doi.org/10.1088/0953-8984/26/43/433202.*

c-axis is aligned parallel to the diagonals of the perovskite cube. In other terms, $[001]_{\text{hexagonal}} \parallel [111]_{\text{pseudocubic}}$. The corresponding hexagonal lattice parameters (Fig. 2.2C are $a_{\text{hex}} = 5.579$ Å and $c_{\text{hex}} = 13.869$ Å [14,18].

Bulk $BiFeO_3$ is a semiconductor with literature values of the bandgap determined by optical measurements at room temperature in the range from 2.1 to 2.8 eV. Several authors claim that $BiFeO_3$ has a direct bandgap transition at about 2.1−2.8 eV [19−22]. There are, however, published studies in which it has been shown that $BiFeO_3$ has an indirect bandgap transition of about 0.4−1.0 eV, quite smaller as compared to the values obtained for the direct transition [23]. Density functional theory calculations [24,25] have corroborated an indirect energy transition of about 2.1 eV, while in the room temperature absorption spectra recorded on $BiFeO_3$ thin film, the transition at approximately 2.17 eV has been observed [26].

Finally, according to Catalan and some of the references therein [16], based on two-probe DC resistivity measurements carried out on high-quality bulk samples of $BiFeO_3$, the log resistivity value undergoes two slopes in Arrhenius law with increasing temperature. Actually, it has been found that the activation energy of the charge carriers decreases from nearly 1.3 down to nearly 0.6 eV as the material is heated above T_N with the anomaly around it. However, one does not expect such type of conducting behavior when the scale of the crystal moves down to several nanometers. Indeed, in the case of defective nanoparticles with a core/shell structure [1], the nanoparticle shell may have metallic and/or semiconducting features, while the nanoparticle core prominently features insulating properties. This casts a shadow over models that are commonly applied in pristine bulk materials to fit the resistivity data in systems with disorder and/or decreased dimensions.

At a scale ranging down to nanometers, $BiFeO_3$ has proven very prospective for a potential use in satellite communications, electrically accessed magnetic memory, commercial applications for photovoltaics and alternative sensors [16]. Most essentially, the electric resistance of $BiFeO_3$ is found to be a key parameter that should comply with the prime industrial requirements. Accomplishing high-electric conductivity value in this nanoscopic compound from its powders is one of the major assets and is perceived as a very promising in development of the novelty. Moreover, it proves quite demanding to identify the charge carrier transport, as well as, to distill electric conductivity value using the contact probes themselves invasively [27,28]. On the other hand, RS tool is widely known as a local and highly informative experimental probe capable of assessing the origin and dynamics of charge carriers in conducting materials. This makes Raman technique a reliable, yet noninvasive, means for investigating the transport properties of materials that are treated with utmost delicacy.

Fairly recent temperature-dependent RS study, carried out on the multiferroic $BiFeO_3$ nanoparticles of high purity and relied on the temperature evolution electronic Raman background [1], has explored an exciting prospect of extracting the relevant piece of information about the electric transport in this nanoscopic compound. μ-RS measurements were recorded over the temperature range of 80−723 K, while the related spectra were gathered at the backscattering arrangement with solid state 532 nm Nd:YAG laser as excitation at sub-mW laser powers on the sample itself. There were more than 13 optical phonon modes (symmetry: A_1 and E) detected in the experiment, while the spectra were decomposed with Lorentzian lineshape profiles, as is presented in Fig. 2.3 at four different temperatures. The entire number, together with frequency positions, of the optically active phonon modes of $BiFeO_3$ nanoparticles detected with Raman were found exactly the same with those observed in temperature-dependent RS spectra undertaken for bulk crystalline $BiFeO_3$ [29]. However, the authors [1] properly commented on the emerged splittings of a number of few polar LO+TO phonon modes, which naturally appear in the case of $BiFeO_3$ nanoparticles [30,31]. As with bulk, the prediction based on the factor group analysis turns out to be in accordance with the experiment implying 13 ($4A_1 + 9E$) optically active modes in phonon Raman spectra [32].

In contrast to Raman spectra recorded for on bulk $BiFeO_3$, Raman active optical modes pertinent to $BiFeO_3$ nanoparticles were evidenced to seat on quite a broad spectroscopic profile (Fig. 2.3 shaded in light gray). Such a spectroscopic feature has a pronounced temperature dependence and is familiarly known as Raman electronic background. In literature, indeed there are spectroscopic backgrounds akin to one studied in Ref. [1] such as nonresonant Raman continuous profile observed in metal-oxide thin films [33]. However, the related profile is quite shapeless, moreover with strong intensity, and is ascribed to entirely electronic RS recoil independent of bands due to the phonons. This Raman electronic background emerges as a result of the surface roughness at atomic scale.

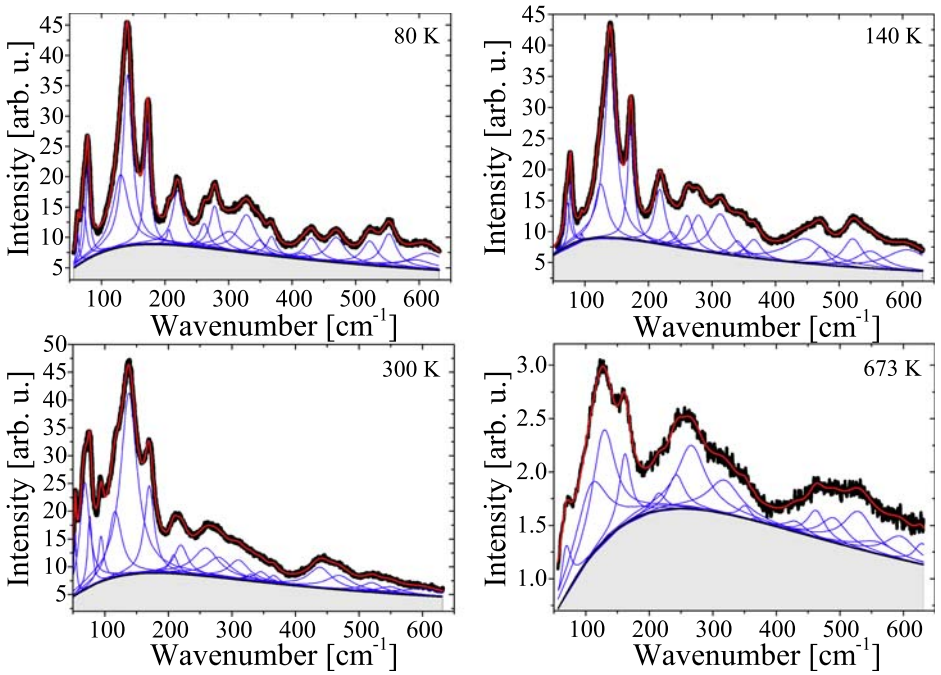

Figure 2.3

Raman scattering spectra given for four representative temperatures (data points presented in black). The spectra are composed of a continuous electronic background (shaded in light gray) and Lorentzian phonon peaks (*lines* in blue). The overall *fitting line* is drawn with *red line*. *The figure is adopted from the published work D.M. Djokić, B. Stojadinović, D. Stepanenko, Z. Dohčević-Mitrović, Probing charge carrier transport regimes in $BiFeO_3$ nanoparticles by Raman spectroscopy, Scr. Mater. 181 (2020) 6–9. https://doi.org/10.1016/j.scriptamat.2020.02.008.*

In addition, it has been reported that, in extremely small metallic particles [34] and metallic thin film islands with adsorbents [35], RS due to the particle-hole pair excitations brings about the emergence of the phononless continuous electronic background. This can be explained in terms of the momentum conservation violation generated in the presence of the electronic states at surface. Furthermore, even in the bulk hole-doped manganese perovskites, the broad electronic Raman response associated with the scattering by conduction electrons has been determined to cause a drastic change at the phase transition, as shown by Liu et al. [36]. The evolution of the effects of electron correlations in this compound could be assessed computably with temperature.

The authors of Ref. [1] have fittingly cast the surface states situated at particle boundaries in the role of localization centers via which the conduction can run efficiently. In terms of energy, these states are located near the vicinity of the Fermi level and they are, in general, unequally distributed to evolve with both spatial and energy gap between them. Therefore, the charge carrier conduction mechanism in which the hopping energy varies

with the hopping range can be safely modeled for description of the transport over an extended temperature range in disordered semiconductors and/or amorphous solids, such as nanoscaled materials. Commonly, exceptionally high-electric resistivity values are observed in such systems. As such, these values serve as a definite fingerprint to rule out any conventional metallic/semiconducting type of conductivity mechanism intrinsic to (semi)conductors. VRH mechanism, nonetheless [37], stands for a rather viable transport mechanism in nanoparticles with no other alternative acceptable, as was reported in Ref. [1] for $BiFeO_3$ nanoparticles. Two different types of VRH charge carrier transport mechanisms in $3D$ have been probed in a contactless way using temperature-dependent Raman spectroscopy, and it has been evidenced that these two are affected by different degrees of the electron correlation strengths on the opposite sides of the antiferromagnetic phase transition. Below the transition temperature, the transport undergoes the mechanism explained by Efros and Shklovskii [38], whereas at high temperatures, the charge carrier transport adheres to the traditional Mott VRH theory [37].

Here we provide a brief account of the Mott and Efros−Shklovskii laws based on a concise analysis from a seminal paper by Arginskaya and Kozub [39]. The central focus of this study was on a considerable diversity of theoretical results emerging from calculations for the exponential prefactors in various VRH expressions, as well as, the crossover from VRH conductivity of Mott type in which the density of electronic states at Fermi level is $g(\varepsilon \approx \varepsilon_F) = const$ toward VRH conductivity running via states separated by a Coulomb gap when $g(\varepsilon \approx \varepsilon_F) \propto \varepsilon^2$. Aharony et al. [40] have made an attempt to obtain the universal analytic expression for the temperature dependence of conductivity, $\sigma(T)$, in the crossover region from Mott to Efros−Shklovskii law. In general terms, temperature dependence of the VRH conductivity $\sigma(T)$ can be written down as

$$\sigma(T) = \sigma_n \exp\left(-\frac{T_n}{T}\right)^n, \tag{2.9}$$

where n might take on $1/4$ or $1/2$ in $3D$ with respect to the law chosen, Mott's or Efros−Shklovskii's. Constant factors σ_n and T_n depend on the preferred of the two models. However, the common feature of most of the relevant studies in the field of VRH boils down to simplistic approaches in estimating the exponential prefactor σ_n. As a traditional rule, σ_n is generally assumed to have no temperature dependence.

Factors σ_n and T_n, which are given in Eq. (2.9), can be computed straightforwardly by optimizing the correlation linking the energy and spatial separation between the lattice sites. Once an electric field is applied, hopping in the direction of the field is rather preferred at different probabilities with respect to both distance and energy separation. As with the $3D$ free electron case, in original Mott paper [37], it was in a simplified way presented that the hopping energy is inversely proportional to the cube of the hopping distance, while the hopping frequency ν for a given temperature T was found to depend on

two following parameters: r as the spatial distance between the sites in units of localization length ξ and W as their typical hopping energy separation. Namely,

$$\nu = \nu_0 \exp\left(-\frac{2r}{\xi} - \frac{W}{k_B T} \right), \tag{2.10}$$

where $\nu \equiv \nu_0$ for both $r = 0$ and $W = 0$, whereas $k_B = 1.38 \times 10^{-23}\ \mathrm{J/K}$ stands for Boltzmann constant. The hopping frequency characterizes the relative number of directed charge carrier hops due to the electric field. Indeed, in noncrystalline systems, the variables r and W are not randomly independent so that one can be combined into a single parameter by minimizing the total exponent in (Eq. 2.10). In the actual fact, the hopping from one site to another with a lower energy/distance occurs at high rate. However, reaching both low energy/distance sites at the same time remains utterly impossible. The same reasoning applies for the large energy/distance sites that altogether justifies the application of variation method and thence the term "variable" in VRH.

Variable hopping processes translate a charge carrier by a range r within a time $\sim 1/\nu$, but at a preferred W value that maximizes the electric current via hopping. This proportionality squarely leads to the VRH expression for conductivity which is given in (Eq. 2.9). Yet, to relate r with W or vice versa, one has to further assume that most of the mobile carriers come from a narrow energy window near the Fermi level of width $\sim k_B T$. In such a way, the carrier density n_c of spin $S = 1/2$ which as the other factor prominently figures in the expression for the conductivity and can be computed by integration as

$$n_c = 2 \int_{\varepsilon_F}^{\varepsilon_F + k_B T} g(\varepsilon) \mathrm{d}\varepsilon, \tag{2.11}$$

where $g(\varepsilon)$ measures the total number of states ($\mathrm{d}N$) per both energy ($\mathrm{d}E$) and volume unit (V), each of which is double degenerated ($2S + 1 = 2$).

One must emphasize that the wise choice of $g(\varepsilon)$ leads to the correct expression for the exponent T_n, which differs by switching from $3D$ Mott ($n = 1/4$) to Efros−Shklovskii regime ($n = 1/2$). Experimental measurements in disordered systems do reveal that the electron density of states (DOSs) may strongly vary in the vicinity of Fermi level, and it seems reasonable to suggest that the theoretical concept of uniform DOSs near the Fermi level is certainly insufficient to describe conduction mechanisms which account for the Coulomb gap, as there is a jump in the electron DOSs due to Coulomb interactions between localized states. In general, one can write down

$$k_B T_n = \begin{cases} c_p / \left(g(\varepsilon_F) \xi^3 \right), & \text{for } n = 1/4 \\ e^2 / (4\pi\varepsilon_0 \varepsilon_r \xi), & \text{for } n = 1/2 \end{cases} \tag{2.12}$$

where $k_B = 1.38 \times 10^{-23}$ J/K and $\varepsilon_0 = 8.85 \times 10^{-12}$ F/m, while ξ stands for the localization length of electron wave function of the surface states. c_p represents the percolation constant varying from 5 to 20. ε_r corresponds to the relative permittivity constant. Nevertheless, even when the DOSs is not constant, the $3D$ Mott VRH conductivity pattern is fully recovered if presented like Eq. (2.9), but is rather referred to as the $3D$ Efros−Shklovskii VRH [38] when n is, in particular, equal to $1/2$. In Ref. [41], a few temperature dependencies of the hopping conductivity, which come under exponent $1/4$ or $1/2$, are presented and the reader is further redirected to this reference to properly infer the validity of use of VRH at high temperatures in disordered materials.

Nanoscaled $BiFeO_3$ puts itself forward as a suitable candidate for exploring the crossover from $1/2$ to $1/4$ exponent VRH conductivity as demonstrated in Ref. [1] based on the Raman spectra. More interesting is the fact that crystalline $BiFeO_3$ nanoparticles do not only undergo a crossover but even a pronounced phase transition at $\sim$640 K below which Coulomb correlations take place to form the antiferromagnetic ordering. Above the transition temperature, however, these correlations become overwhelmed by the temperature fluctuations through the concrete manifestation of the metallic-like paramagnetic state.

There is a presence of localized surface states occupying the energies near the Fermi level in the $BiFeO_3$ nanomaterial. These states through a mediation back the VRH transport even over a broad range of temperature. Temperature variations of $\ln(1/\tau)$, which is proportional to $\ln(\sigma)$ based on the Einstein relation from Eq. (2.8) are linearized against T^{-n} in Fig. 2.4A with $n = 1/2$ and Fig. 2.4B with $n = 1/4$, in the strongly correlated ($T < T_N$) and paramagnetic phase ($T > T_N$), respectively. Relying on the calculation for $\varepsilon_r \approx 28$ from the impedance dielectric spectroscopy of $BiFeO_3$ nanoparticles [42] and following (12) one can find that $\xi \approx 7$ nm, while the DOSs $g(\varepsilon_F)$ in the high-temperature phase nearly amounts 2.1×10^{18} localized states per (eV $\times$ cm^3). The result $\xi \approx 7$ nm is physically meaningful since $\xi < \langle \ell \rangle$, where the average particle size $\langle \ell \rangle \approx 66$ nm has been computed from the Gauβian particle size distribution recorded by Scanning Electron Microscopy at room temperature on $BiFeO_3$ (Fig. 2.4C and D). Finally, $\rho = 1/\sigma \approx 4\pi^2\tau/\left(\langle \ell \rangle^2 e^2 g(\varepsilon_F)\right) \approx 350$ mΩcm, which stands for an extraordinarily high value that is not commonly encountered in conventional metals. This value goes beyond the maximum resistivity value ($\sim$1 mΩcm) limited by the Mott-Ioffe-Regel criterion [43,44], which categorizes crystalline $BiFeO_3$ nanoparticles into a family of bad conductors and ultimately suggests that the conduction bands are vanishing. This eliminates any possibility for the fixed thermally activated transport generic to intrinsic semiconductors to dominate over $3D$ VRH.

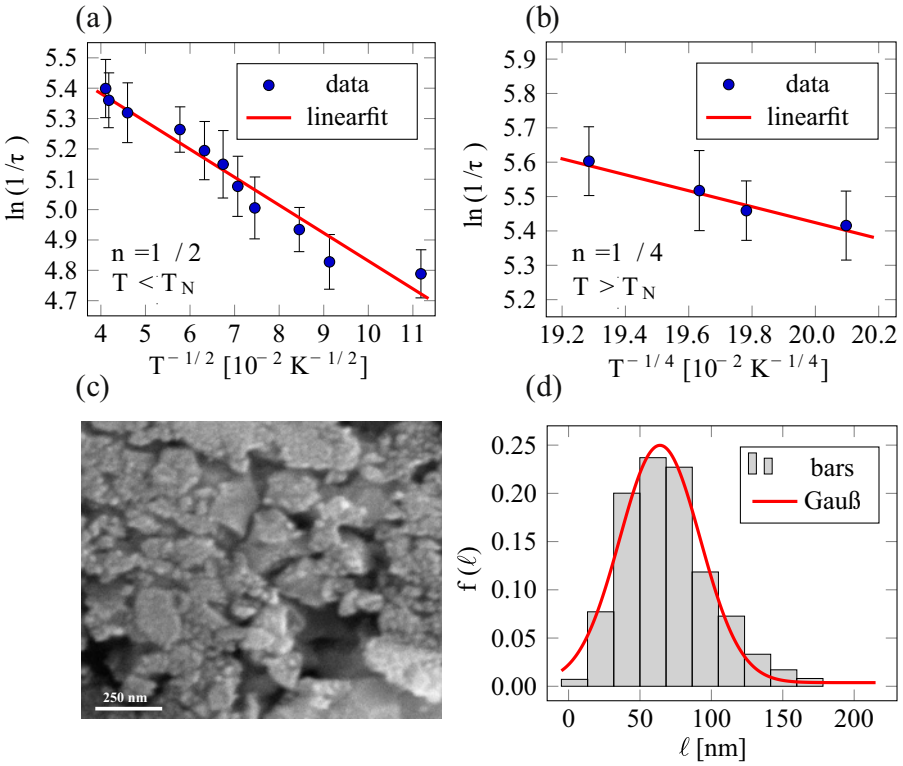

Figure 2.4

The dependence (T^{-n}) versus ($\ln(1/\tau)$) in both paramagnetic phase (subfigure (A), $n = 1/2$) and antiferromagnetic phase (subfigure (B), $n = 1/4$) with the linear fitting curves given in red. The surface morphology of the nanocrystalline $BiFeO_3$ particles made with TESCAN SM-300 (subfigure (C)) and the corresponding histogram of the distribution of the particle size given in gray, fitted by the Gauβ distribution (red line), where (64 ± 2) nm is mean value and (28 ± 2)nm is standard deviation (subfigure (D)). The frequency of occurrence is labeled as $f(\ell)$. *The entire figure is taken from D.M. Djokić, B. Stojadinović, D. Stepanenko, Z. Dohčević-Mitrović, Probing charge carrier transport regimes in $BiFeO_3$ nanoparticles by Raman spectroscopy, Scr. Mater. 181 (2020) 6–9. https://doi.org/10.1016/j.scriptamat.2020.02.008.*

In certain disordered semiconductors, Ioffe and Regel [45], as well as Mott [46], have altogether realized that conduction states pertinent to such systems fail to survive due to the indefinite reduction in free mean path of carriers that scatters by. The key argument is that it can never become shorter than the typical interatomic spacing. In this case, the concept of carrier velocity cannot be properly formulated, and the entire coherent quasiparticle motion is lost. The notion of a minimum metallic conductivity is actually in accordance with a minimum mean free path.

Generally, the choice of 3*D* VRH ought to be provisionally accepted as an assumption. In the case of $BiFeO_3$ nanoparticles, the existence of the Mott VRH mechanism has already been deduced from the DC/AC measurements. These results are presented in Ref. [27]. Furthermore, the assumption about the validity of VRH is substantiated by the fact that the estimated resistivity value ultimately exceeds the Mott-Ioffe-Regel maximum ($350\ m\Omega cm \gg 1\ m\Omega cm$). This implies that the conduction band energy sector tends to fade away leaving no room for the fixed thermally activated transport to prevail, which typically requires a markedly high density of conduction band states. Therefore, the $BiFeO_3$ nanoparticles are safe to be termed as bad conductors that retain metallic behavior, through qualitative features such as temperature evolution. Quantitatively, however, the bad conductors very much resemble the electric insulators as was observed in Ref. [1]. Specifically, the $BiFeO_3$ nanoparticle shell exhibits metallic behavior whereas the core insulator one, which is a case in defective nanoparticles with a core/shell structure.

3. Infrared reflection

3.1 Short introduction to infrared reflection technique

Infrared solid state spectroscopy stands for one of the most powerful and versatile techniques meant for optically probing a diverse family of materials in a contactless manner. The IRR response can assume either a purely electronic or a purely LV character. The two cases have distinctly different approaches to the quantitative treatment of the interaction processes between the radiation field and matter. The latter has conclusively proven powerful for analyzing propagating vibrations with which crystal structures can be revealed in ionic crystals and polar semiconductors. This analytical probe is highly useful even for systems poor in the degree of crystallinity, which is oftentimes encountered in nanoscopic matter.

In the long-wave limit ($q \approx 0$), optically active vibrations of an ionic bipartite lattice encapsulate the motion of one type of atoms relative to that of the other sublattice, yet both in spatial phase. The natural concomitants of such motions comprise strong electric dipoles of the material that can, accordingly, be directly coupled with the external electric field at a given polarization angle of the incident electromagnetic radiation. The theory of the IRR response originating form the interaction between the radiation field and the matter is purely phenomenological and can be found elsewhere [4,47,48], based on Maxwell's and the macroscopic equations describing the vibrations in a polar material. The reflective IRR spectroscopic recoil begins with a singularity in the dielectric function observed at the transverse optical (TO) frequency of the polar phonon mode. The singularity occurs as the radiation field of the incident electromagnetic wave couples with the TO phonon mode. Coulombic force effects in the polar crystal shift the LO mode to higher energies in contrast to the TO mode. The TO mode has a complex pole of the

complex dielectric response function $\widetilde{\varepsilon}(\omega)$, whereas the LO mode is associated with a complex zero of $\widetilde{\varepsilon}(\omega)$. Consequently, the incident infrared electromagnetic waves at frequencies over the so-called *reststrahlen* TO-LO window are dispersed in such a way that they fail to propagate through the condensed medium, but undergo reflection. In an ideal polar crystal with undamped oscillators, the frequency selective reflectivity amounts exactly 100%, but the reality is rather followed with the oscillator damping. Formally, the reflectivity is given by the Fresnel formula

$$R(\omega) = \left|\frac{\widetilde{n}(\omega) - 1}{\widetilde{n}(\omega) + 1}\right|^2 = \frac{(n(\omega) - 1)^2 + \kappa^2(\omega)}{(n(\omega) + 1)^2 + \kappa^2(\omega)}, \tag{2.13}$$

where $R(\omega)$ is the frequency-dependent fraction of light intensity reflected. Complex frequency dependent index of refraction, $\widetilde{n}(\omega)$, is related to the complex dielectric response as

$$\widetilde{n}(\omega) = n(\omega) - i\kappa(\omega) = \sqrt{\widetilde{\varepsilon}(\omega)}. \tag{2.14}$$

The frequency dependent real part, $n(\omega)$, and imaginary part, $\kappa(\omega)$ as the extinction coefficient, of the complex refractive index $\widetilde{n}(\omega)$ satisfy the following relationships

$$\varepsilon_1(\omega) = n(\omega)^2 - \kappa(\omega)^2 \quad \text{and} \quad \varepsilon_2(\omega) = 2n(\omega)\kappa(\omega), \tag{2.15}$$

where finally

$$\widetilde{\varepsilon}(\omega) \equiv \varepsilon_1(\omega) + i\varepsilon_2(\omega). \tag{2.16}$$

For this reason, it is of uppermost importance to model, as well as, parametrize $\widetilde{n\varepsilon}(\omega)$ that properly describe the system probed by the IRR technique.

IRR signal of poorly conductive ionic crystals with large splitting between TO and LO frequencies is commonly fitted with a complex dielectric function given by the following expression

$$\widetilde{\varepsilon}(\omega) = \varepsilon_\infty \prod_j \frac{\omega_{\mathrm{LO}j}^2 - \omega^2 + i\omega\gamma_{\mathrm{LO}j}}{\omega_{\mathrm{TO}j}^2 - \omega^2 + i\omega\gamma_{\mathrm{TO}j}}, \tag{2.17}$$

where $\omega_{\mathrm{LO}j}$ and $\omega_{\mathrm{TO}j}$ are longitudinal and transverse frequencies of the j-th oscillator, respectively, while $\gamma_{\mathrm{TO}j}$ and $\gamma_{\mathrm{LO}j}$ are their energy dampings, and ε_∞ corresponds to the high-frequency dielectric constant ($\omega \to \infty$). This model presents four tunable parameters for each TO/LO mode and is employed for description of purely phononic spectra. The model is familiarly known as the LV model, or habitually, four-parameter factorized form of the dielectric function. Its major disadvantage consists in the fact that it considers no contribution from the itinerant electronic excitations, neither single particle nor collective [49].

However, a great deal of semiconductors has a sizable portion of itinerant charge carriers. Accordingly, the full description of the infrared optical reflectivity data of such materials has to allow for both phonon and electronically collective (plasmon) excitations. The cohabitation between the phonons and plasmons brings inexorably about a somewhat pronounced interaction between the plasmons and LO phonons. This effect becomes the most striking if the plasma frequency ω_P lies situated close to the LO phonon energy. In this case, the complex dielectric function [50] can be factorized to read as follows

$$\widetilde{\varepsilon}(\omega) = \varepsilon_\infty \frac{\prod_{j=1}^{m+n}\left(\omega^2 + i\omega\gamma_{\mathrm{LO}j} - \omega_{\mathrm{LO}j}^2\right)}{\omega^m \prod_{j=1}^{m}\left(\omega + i\gamma_{P_j}\right)\prod_{j=1}^{n}\left(\omega^2 + i\omega\gamma_{\mathrm{TO}j} - \omega_{\mathrm{TO}j}^2\right)}, \tag{2.18}$$

where $\omega_{\mathrm{TO}j}$ and $\gamma_{\mathrm{TO}j}$ are frequencies and damping of the TO modes, respectively. γ_P represents the plasma damping rate. The equation directly expresses the coupled plasmon-LO phonon frequencies $\omega_{\mathrm{LO}j}$ and damping rates $\gamma_{\mathrm{LO}j}$. This model is in literature termed as the coupled plasmon-phonon (CPP) model.

In conducting oxides [48], on the other hand side, the Drude model can be employed with no coupling for fitting the infrared reflectivity spectra. The plasmon contribution to the complex dielectric function is expressed through the Drude term so that $\widetilde{\varepsilon}(\omega)$ is composed of two additive terms in the following manner

$$\widetilde{\varepsilon}(\omega) = \varepsilon_\infty \left(\prod_j \frac{\omega_{\mathrm{LO}j}^2 - \omega^2 + i\omega\gamma_{\mathrm{LO}j}}{\omega_{\mathrm{TO}j}^2 - \omega^2 + i\omega\gamma_{\mathrm{TO}j}} - \frac{\omega_P^2}{\omega(\omega - i\gamma_P)} \right). \tag{2.19}$$

The first product term is concerned with the pure phonon contribution, while the second term represents the contributions originating from the collective electronic excitations—plasmons. The $\omega_{(\mathrm{TO/LO})j}$ and $\gamma_{(\mathrm{TO/LO})j}$ are (TO/LO) frequencies and the related damping rates of the decoupled phonon modes. The ω_P and γ_P are the plasma frequency and its daping rate. This model brings us a material advantage in decoupling the phonon from the plasmon contributions, and is called the decoupled plasmon-phonon (DPP) model. Besides the aforementioned "classical" Drude term, sometimes the so-called Double-damped Drude term is used, as is given in

$$\widetilde{\varepsilon}(\omega) = \varepsilon_\infty \left(\prod_j \frac{\omega_{\mathrm{LO}j}^2 - \omega^2 + i\omega\gamma_{\mathrm{LO}j}}{\omega_{\mathrm{TO}j}^2 - \omega^2 + i\omega\gamma_{\mathrm{TO}j}} - \frac{\omega_P^2 + i(\gamma_P - \gamma_0)\omega}{\omega(\omega - i\gamma_0)} \right). \tag{2.20}$$

The difference between the dynamic damping (γ_P) at plasma frequency and the static damping (γ_0) at zero frequency represents particular distinctiveness of this model. The second term in the additive form of $\widetilde{\varepsilon}(\omega)$ turns into the classical Drude term once

$\gamma_P = \gamma_0$. The use of this model, which is also called DPP, provides more flexibility. In fact, a rather precise description of the parametrized complex dielectric function is offered by the model in numerical fittings based on it.

As with nanomaterials, the related IRR spectra can be properly analyzed using the Bruggeman effective medium approximation [51]. The basic Bruggeman model includes the influence of porosity as

$$\left(\frac{\widetilde{\varepsilon}(\omega) - \widetilde{\varepsilon}_{\text{eff}}\ (\omega)}{\widetilde{\varepsilon}(\omega) + 2\widetilde{\varepsilon}_{\text{eff}}\ (\omega)}\right)\widetilde{f} + \left(\frac{1 - \widetilde{\varepsilon}_{\text{eff}}\ (\omega)}{1 + 2\widetilde{\varepsilon}_{\text{eff}}\ (\omega)}\right)\left(1 - \widetilde{f}\right) = 0. \tag{2.21}$$

A decrease of the powder volume fraction as compared to the ambient air leads to a decrease in the reflectivity values, and thence the IRR features may become significantly broadened if there is a greater air fraction in the powder. For the binary material with a great degree of inhomogeneity, constituted of the material $\widetilde{\varepsilon}(\omega)$ and air ($\varepsilon_{\text{air}} = 1$) with the volume fractions $\widetilde{f}$ and $1 - \widetilde{f}$, respectively, the empirical relation for the complex effective dielectric function $\widetilde{\varepsilon}_{\text{eff}}\ (\omega)$ must obey the above-written equation.

3.2 Doped nanocrystalline CeO_2

As one of the most stable oxide of cerium, cerium dioxide CeO_2 is considered to be highly important functional material with outstanding applications in many various fields. It crystallizes into a fluorite face centered cubic structure with space group F_{m3m} (No. 225) to form a simple cubic oxygen suba lattice where the cerium ions occupy alternate cube centers (see Fig. 2.5A) [52]. In terms of Wyckoff positions, Ce atoms are located at the centers of the tetrahedrons (4a) (0,0,0) of which corners are populated with

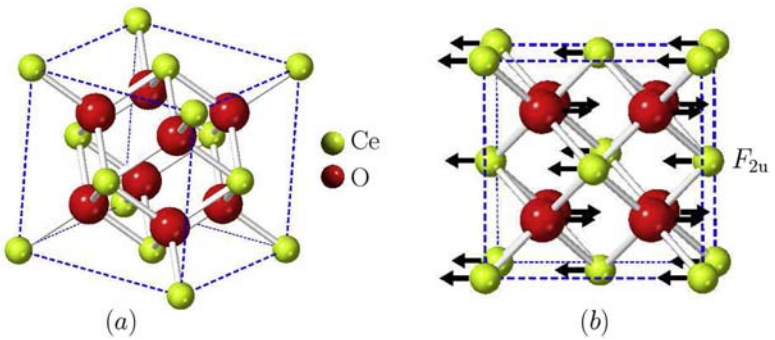

Figure 2.5
The fluorite face centered cubic crystal structure of CeO_2 (A) and its normal mode of the infrared active lattice vibrations of (B). Ce ions are denoted in green, while O ions are denoted in red.

oxygen ions (8c) (1/4, 1/4, 1/4). Observing the existence of the center of inversion, the structure has exactly one IRR (F_{2u}) and one Raman (F_{2g}) active mode [32], both of which are triple degenerated. As is shown in Fig. 2.5B, the normal mode of the infrared optically active vibrations consist of motions of both Ce and O atoms, but in the opposite directions.

Nanocrystalline CeO_2 is distinguished by its enhanced electric conductivity, size lattice relaxation, as well as, many other advantages to bulk CeO_2. As to what has been reviewed in Ref. [53], decreasing particle size of crystalline CeO_2 particles down to nanoceria dioxide crystals results in the formation of oxygen vacancies which can be further employed as descriptors for determining the valence state of Ce in the nanoparticles. Actually, the large surface to volume ratio, then the inclination toward the oxygen consumption, and basically, freeing Ce because of the reversible transition between Ce^{3+} and Ce^{4+} ions altogether lead to enormous catalytic capacity of this material. Nanoscaled CeO_2 is furthermore found applicable to the active area of research for renewable energy, solid oxide fuel cells, water and air purification, optical glass polishing and decolorizing, UV ray filters, and many others [53].

Doped nanocrystalline CeO_2, however, deserves a special attention as the optimal doping with Cu or Nd has proven efficient in inducing the semiconductor-to-metallic state crossover [2,52] in nanoceria dioxide. Moreover, electrons localized at the vacancies may behave like free charge carriers to contribute drastically to the electrical conductivity [54]. This originates from the presence of free charge carriers, which are numbered in the nanoceria lattice, as the number of oxygen vacancies becomes increased by Nd content [55].

Following Ref. [2], the IRR spectroscopy has been applied to nondestructively investigate the mechanism of the influence of the plasmon due to the enhanced conductivity upon the phonon spectra with increasing Nd content in nanocrystalline CeO_2 This material is a polar semiconductor so that both phonon and plasmon excitations can be registered in the IRR spectra, whereby the plasmon-phonon coupling mechanism can be explored, while the extent to which the system acquires metallicity can be assessed. Radović et al. [2] have recorded the infrared reflectivity spectra on pure and Nd-doped CeO_{2-y} nanopowders at ambient temperature in far-infrared region from 100 up to 700 cm^{-1}.

Fig. 2.6 shows the IRR spectra of undoped and Nd-doped CeO_{2-y} nanopowders fitted with the two models: coupled plasmon-phonon and decoupled plasmon-phonon with double-damped Drude term. The concentration of the dopant is increased from 0% to 25%. The IRR spectra markedly differ from those done on bulk CeO_2, as the bulk reststrahlen region is split into two extended TO-LO modes over 200−550 cm^{-1} range with decreasing crystallite size. The splitting is more pronounced in samples with rather small crystallite sizes and is accompanied with the redshift of the two LO modes, as well. Also, one can

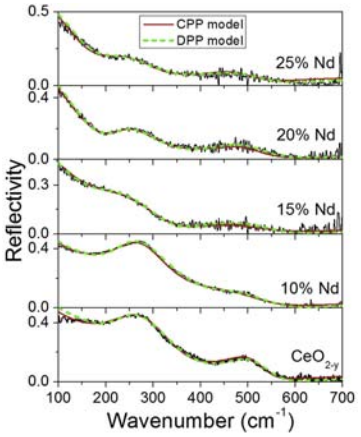

Figure 2.6

Infrared reflectivity spectra of undoped and Nd-doped CeO_{2-y} nanopowders involving the two theoretical fits based on coupled plasmon-phonon and decoupled plasmon-phonon model. *The credits for the figure are given to M. Radović, Z. Dohčević-Mitrović, N. Paunović, S. Bošković, N. Tomić, N. Tadić, I. Belča, Infrared study of plasmon-phonon coupling in pure and Nd-doped CeO_{2-y} nanocrystals, J. Phys. D Appl. Phys. 48 (2015) 065301–065306. https://doi.org/10.1088/0022-3727/48/6/065301.*

notice that with the raise of the dopant concentration, the low energy Drude tail and the screening of the phonon modes became more and more prominent, due to the strong presence of the free charge carriers. In the actual fact, increasing Nd content in the nanoceria dioxide lattice can generate a huge number of oxygen vacancies [2], while the plasmon-phonon interaction in the Nd-doped samples gets stronger.

Following the fits based upon both models applied (Fig. 2.6), all the plasmon modes registered in all nanoceria dioxide samples exhibit a frequency decrease with Nd doping, as can be seen from Fig. 2.7. The shift in the plasma frequency toward lower energies with increasing Nd concentration occurs owing to the weighted effective charge carrier mass, as there is no dopant impact on the free carrier concentration [2]. In fact, the plasma frequency is inversely proportional to the effective electron mass. This feature, together with the enhanced plasmon-phonon coupling with Nd doping, affords us a better insight into the transport properties of crystalline nanoceria based on the infrared-derived optical conductivity [48].

4. Electron spin resonance

4.1 Short introduction to electron spin resonance technique

ESR exemplifies a very sensitive and informative experimental technique, based on the use of magnetic field, which continues to find countless applications not only in solid state and

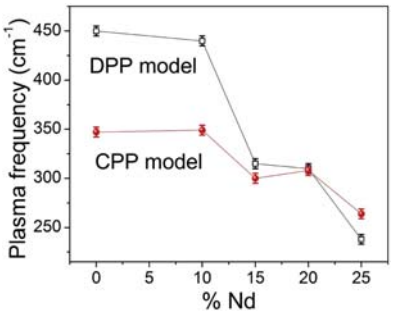

Figure 2.7

Evolution of the plasma frequency with the increased Nd dopant concentration as inferred from the two models: coupled plasmon-phonon and decoupled plasmon-phonon. *The credits for the figure are given to M. Radović, Z. Dohčević-Mitrović, N. Paunović, S. Bošković, N. Tomić, N. Tadić, I. Belča, Infrared study of plasmon-phonon coupling in pure and Nd-doped CeO_{2-y} nanocrystals, J. Phys. D Appl. Phys. 48 (2015) 065301–065306.* https://doi.org/10.1088/0022-3727/48/6/065301.

nano, but also in biomedical and environmental sciences. By means of ESR spectroscopy, one is able to directly probe electron spin response at resonance that certainly makes ESR as one of the most powerful probe to investigate magnetic properties in various compounds. More interestingly, ESR stands for both noninvasive and contactless tool with ability to analyze accurately the nature and dynamics of charge carriers in conductive systems no matter how their geometry welcomes electrical leads and contacts in an electrical circuit.

Familiarly known as CESR in abbreviated term, conduction electron spin resonance has captivated much scientific attention for its capacity to measure the electrical conductivity of systems from bulk over microsized down to nanoscopic conducting materials. In the actual fact, in the conducting systems, the free electron motion exerting eddy current leaves an impact upon the recorded signal at resonance through asymmetry as the definite signature. This was originally recognized by Feher and Kip [56], Dyson [57] who put forward that asymmetric CESR lineshapes originate as linear combinations due to the two facts: (1) the attenuation of the AC field through the skin depth and (2) the capability of itinerant electrons to diffuse backward and forward through the skin depth region in many instances between consecutive spin flips that is only critical to transmission-based CESR techniques. In the case of transmissive CESR, magnetization can penetrate far deeply into metals unlike the AC magnetic field. This gives an extra contribution to enhancing the asymmetry of the signals at resonance [58,59].

Dating back to the 1950′s, Freeman John Dyson is the first in the field to be credited with fully deriving the asymmetric CESR profiles. For the obvious reasons, such CESR lines are referred in literature to as Dysonians of which asymmetry extent is oftentimes quantified using A/B ratio (see the inset in Fig. 2.8), as common signature of metallicity in CESR experiments.

As with CESR operating in the reflection mode, Chapman et al. [61] developed an approach based on Dyson's theory to grasp both on- and off-resonance signal for the various crystal shapes, such as flat plates, long cylinders, and spheres. This allows the prediction of the asymmetric nature of CESR absorption profiles depending on geometry of the conducting samples with different size. Furthermore, Platzman and Wolf [62] examined spin waves excitations at resonance in paramagnetic metals that are described within the frame of Fermi-liquid theory. Their extended theory boils down to Dyson's in the limit of short momentum relaxation times. Dyson's theory was additionally generalized to involve various shapes of conducting crystals at desirable resonant magnetic field directions [63–65]. Later on, Kaplan pointed out that there is a substantial discrepancy between Dyson's theory and experimental results recorded in CESR based on the reflection mode [66]. Actually, CESR becomes recoiled rather with electric than magnetic component of the frequency-dependent electromagnetic field. The component of electric field is known to get easily coupled with the free electron momentum across the surface via relativistic spin-orbit interaction. This fact finds its application in the quantum mechanical density matrix method, which ultimately brings about the rather general form of CESR signal as [67]:

$$\chi''(\omega)\cos\phi + \chi'(\omega)\sin\phi. \tag{2.22}$$

Terms χ'' and χ' represent the absorptive and dispersive parts of the CESR signal. The magnitudes of their contributions are measured with $\cos\phi$ and $\sin\phi$, respectively, both of which disappear in the limit of highly conductive samples, where ϕ is the signal phase. Eq. (2.22) does represent a particular manifestation of Dysonian, which falls into the range of the so-called "NMR limit" [68,69]. In that case, the electron diffusion rate is considerably slower as compared to the spin relaxation rate, and there is no need to consider other limits so as to reasonably infer CESR spectra of usual metallic samples. Spin dynamics itself as regards this case can lead to nothing but Lorentzian-profiled absorptions (χ''), unlike the situations with reduced dimensionality or motionally narrowed signals [70,71].

In a recent CESR study [60], the authors have favored Kaplan's approach, made for analyzing the CESR lineshape, to impart a valuable piece of information on the conductivity of samples with different geometries. Key lengths and points of CESR lines, necessary for simplification of a fitting procedure of CESR lineshape, have been established in this account to analytically derive, as well as, grasp the geometry independent asymmetry ratio limit $A/B \rightarrow (5+3\sqrt{3})/4$, encountered in literature as universal 2.55 limit, when the CESR is carried out on extremely conducting samples. A/B ratio value markedly evolves once nano- or microsized metallic samples start to agglomerate into larger ones that makes the CESR technique especially helpful in

monitoring the extent to which the clustering takes place [72,73]. Moreover, in Ref. [60], the phase dependence of the asymmetry ratio A/B is given as

$$A/B = \frac{\left(1+2\cos\frac{2\phi}{3}\right)\left(3\cos\left(\frac{\pi}{6}-\frac{\phi}{3}\right)+\sin\phi\right)}{4\cos\left(\frac{\pi}{6}-\frac{\phi}{3}\right)\left(1+\sin\left(\frac{\pi}{6}-\frac{2\phi}{3}\right)\right)^2}, \tag{2.23}$$

which can be further employed to relate A/B with the conductivity. Namely, Chapman et al. [61] introduced the parameter $\eta \equiv d/\delta$, where d represents the characteristic length od the sample (thickness or diameter), while δ is the skin depth at given resonant frequency. It is exactly this quantity that is in correlation with the sample conductivity. The absorptive and dispersive parts of the CESR signal in Ref. [61] are respectively $x(\eta)$ and $y(\eta)$ so that $y(\eta)/x(\eta)$ exactly corresponds to $\tan\phi$ in Ref. [60]. According to Ref. [61], $x(\eta)$ and $y(\eta)$ for the three relevant geometries look like

$$\text{Plate} \Rightarrow \begin{cases} x(\eta) = \dfrac{\sinh(\eta)+\sin(\eta)}{2\eta(\cosh(\eta)+\cos(\eta))} + \dfrac{1+\cosh(\eta)\cos(\eta)}{(\cosh(\eta)+\cos(\eta))^2}, \\ y(\eta) = \dfrac{\sinh(\eta)-\sin(\eta)}{2\eta(\cosh(\eta)+\cos(\eta))} + \dfrac{\sinh(\eta)\sin(\eta)}{(\cosh(\eta)+\cos(\eta))^2}. \end{cases} \tag{2.24}$$

$$\text{Cylinder} \Rightarrow \begin{cases} x(\eta) = 1 - \dfrac{2(\text{Ber}(\vartheta)\text{Ber}'(\vartheta)+\text{Bei}(\vartheta)\text{Bei}'(\vartheta))(\text{Ber}(\vartheta)\text{Bei}'(\vartheta)-\text{Ber}'(\vartheta)\text{Bei}(\vartheta))}{\left(\text{Ber}^2(\vartheta)+\text{Bei}^2(\vartheta)\right)^2}, \\ y(\eta) = \dfrac{\left(\text{Ber}^2(\vartheta)-\text{Bei}^2(\vartheta)\right)\left(\text{Bei}'^2(\vartheta)-\text{Ber}'^2(\vartheta)\right)-4\text{Ber}(\vartheta)\text{Bei}(\vartheta)\text{Ber}'(\vartheta)\text{Bei}'(\vartheta)}{\left(\text{Ber}^2(\vartheta)+\text{Bei}^2(\vartheta)\right)^2}, \\ \text{where } \vartheta \equiv \eta/\sqrt{2}. \end{cases} \tag{2.25}$$

$$\text{Sphere} \Rightarrow \begin{cases} \dfrac{4}{9}x(\eta) = \dfrac{8+\eta^4}{\eta^4} - \\ \dfrac{8(\sinh(\eta)+\sin(\eta))}{\eta^3(\cosh(\eta)-\cos(\eta))} + \dfrac{8\sinh(\eta)\sin(\eta)}{\eta^2(\cosh(\eta)-\cos(\eta))^2} + \dfrac{\sinh(\eta)-\sin(\eta)}{\eta(\cosh(\eta)-\cos(\eta))} - \dfrac{\sinh^2(\eta)-\sin^2(\eta)}{(\cosh(\eta)-\cos(\eta))^2}, \\ \dfrac{4}{9}y(\eta) = \\ \dfrac{8(\sinh(\eta)-\sin(\eta))}{\eta^3(\cosh(\eta)-\cos(\eta))} - \dfrac{4\left(\sinh^2(\eta)-\sin^2(\eta)\right)}{\eta^2(\cosh(\eta)-\cos(\eta))^2} + \dfrac{\sinh(\eta)+\sin(\eta)}{\eta(\cosh(\eta)-\cos(\eta))} - \dfrac{2\sinh(\eta)\sin(\eta)}{(\cosh(\eta)-\cos(\eta))^2}. \end{cases} \tag{2.26}$$

This set of the three dependencies allows us to compute A/B versus $\log\eta$ as is presented in Fig. 2.8. Oftentimes, A/B can be expended in the form of the linear approximation with respect to either η or is proportional to the conductivity of the probed spins. The latter approximation works well in the case of the carbon nanotubes [3] of which CESR-based charge carrier transport is going to be discussed in detail throughout the upcoming section.

4.2 Carbon nanotubes

As a building brick that takes fascinating variety of forms such as diamond, fossil fuels, and graphite, together with innumerable compounds derived from it, carbon stands for one of the most impressive elements in the periodic table. Increased focus of renewed scientific interest in carbon has stepped into the realm of novel carbon-based materials, specifically known as the carbon allotropes at nanoscopic level, such as carbon nanotubes. These were first discovered as multiwalled forms by Iijima in 1991 [74] initiating the golden era of the physics and chemistry of carbon nanostructures. Carbon nanotubes are distinguished by their outstanding electronic, mechanical, and transport properties revealing uncorrelated (semi)conducting nature of the tubes in relation to the curvature and chirality. They also prove suitable for various applications which spam from the use as light and electron emitters [75] up to optical biosensors for life sciences and biomedicine [76].

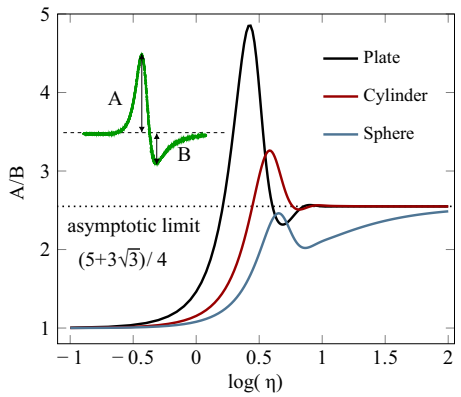

Figure 2.8

Asymmetry ratio A/B dependence on $\log(\eta)$ regarding the three relevant geometries: infinite plate (black), long cylinder (dark red), and sphere (dark blue). All the three curves converge to the asymptotic A/B ratio of $(5+3\sqrt{3})/4$ at $\eta \to \infty$. The inset represents graphically the A/B ratio in an arbitrarily selected CESR line. *The figure is adopted from D.M. Djokić, D. Stepanenko, Z. Dohčević-Mitrović, Extreme conduction electron spin resonance: $A/B \to (5+3\sqrt{3})/4$, the universal limit of lineshape asymmetry ratio, J. Magn. Magn. Mater. 491 (2019) 165616. https://doi.org/10.1016/j.jmmm.2019.165616.*

Even with the aid of nanoscaled technologies, making ideal electric contacts to adequately probe nanotube conductivity remains a perplexing puzzle. Electron backscattering, imbalanced injection of incident electron modes, and high-ohmic contact resistance are identified as the chief culprits at minuscule dimensions. However, nanotubes with large diameters have the added advantage of favoring low-ohmic contact resistance in a four-probe electric measurement [77]. This made them perfectly suited for the investigation of quantum interference caused by the Aharonov−Bohm effect specific by the pronounced magneto-resistance oscillations as a function of magnetic flux [78].

Despite their short diameters, transport electric properties of multiwalled nanotubes oftentimes remain consistent with theoretical models used to describe disordered conductors in $2D$. This might be explained by the fact that the electron wavelength is quite smaller than the nanotube diameter [79]. On the other hand side, one-dimensional essence of carbon nanotubes becomes already evident through specific heat and thermal lattice conductivity measurements since the phonon wavelength exceeds typical nanotube diameters [80], unlike the before-mentioned electron wavelength. Moreover, according to Ref. [81], it has been demonstrated that the electric transport in single walled carbon nanotubes exhibit a dependence in agreement with Luttinger liquid models.

Temperature and power-dependent CESR on an ensemble of metallic SWCNTs have been performed to infer their transport properties based on the insights into the spin dynamics [3]. The powder-form samples comprised acid-purified laser-oven SWCNTs which were prepared using the standardized annealing procedure, while the related CESR spectra were recorded as a function of temperature from 3.4 K to the ambient temperature at the X-band spectrometer. To yield a rather detailed insight into the transport mechanism, the authors of Ref. [3] studied the temperature evolution of the asymmetry Dysonian line shape parameter, $\alpha \equiv A/B$, which is to the first order approximation proportional to the conductance of the probed electron spins. These can relax by interaction with itinerant electrons that are present in metallic SWCNTs. In addition, the spin dephasing rate at resonance narrows with increasing temperature, which is a signature of the motional narrowing, a phenomenon that is particular to metallic systems.

Temperature dependence of the natural logarithm of conductivity, $\ln(\sigma)$ which in this case boils down to $\ln(\alpha)$, is oftentimes plotted versus n-th root of inverse temperature [41]. Exponent n provides information on the charge carrier transport mechanism and when n approaches $1/4$, it leaves a hallmark of 3D Mott VRH transport mechanism [37].

As shown in Fig. 2.9, the Dysonian asymmetry parameter tends to follow a three-dimensional variable-range hopping behavior at low T. From the scaling relationships in Eq. (2.12), the localization length of the electronic wave function, ξ, is roughly estimated to be $\sim$100 nm, whereas the DOSs $g(\varepsilon_F)$ amounts $\sim 10^{19}$ localized states per (eV $\times$ cm^3)

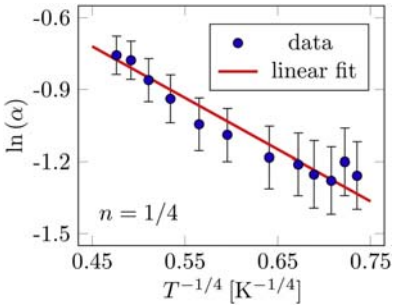

Figure 2.9

Natural logarithm of the asymmetry parameter, $\alpha \equiv A/B$, graphed versus the fourth root of inverse temperature. The logarithm is found to undergo the 3D VRH mechanism. *The data are taken from W.D. Rice, R.T. Weber, P. Nikolaev, S. Arepalli, V. Berka, A.L. Tsai, J. Kono, Spin relaxation times of single-wall carbon nanotubes, Phys. Rev. B 88 (2013) 041401–041405. https://doi.org/10.1103/PhysRevB.88.041401.*

around the Fermi energy. The traditional four-point probe transport measurements on the similarly prepared SWCNT samples [3] have, to some extent, corroborated the present picture of the CESR observed 3D VRH at low *T*.

As with nanoscopic systems such as SWCNTs, one can even venture to state that the VRH conduction mechanism, owing to the localized edge/surface states positioned around Fermi level, may extend even over a wide range of temperatures [1]. At high temperatures, the conduction mechanism in bulk systems commonly runs intrinsically via thermal activation through conduction bands. On the other hand side, there are, as a rule, defect states across the nanotube surface, effectively making its pristine length quite short and comparable to nanoscaled dimensions (Fig. 2.10). In this case, the overlaps between the orbitals decrease to cause the bands to become less dense. This leads to the band splittings to eventually open up wide gaps at rather high energies. Bands that are high in energy have, therefore, tendency to fade away so does the conduction band, as contrary to an ideally pristine SWCNT. It is thus reasonable to adopt that VRH mechanisms may apply up to somewhat higher temperatures in defected nanotubes. Certainly, the intrinsic thermally activated transport via conduction band can be ignored comparing to the VRH due to the evanescent DOSs, as is given in Fig. 2.10.

5. Concluding remarks

In summary, noncontact measurements of transport have been evidenced to offer various advantages to studying novel nanoscopic materials such as: multiferroic crystalline $BiFeO_3$ nanoparticles, doped nanocrystalline CeO_2 used for fuel cell applications, as well as,

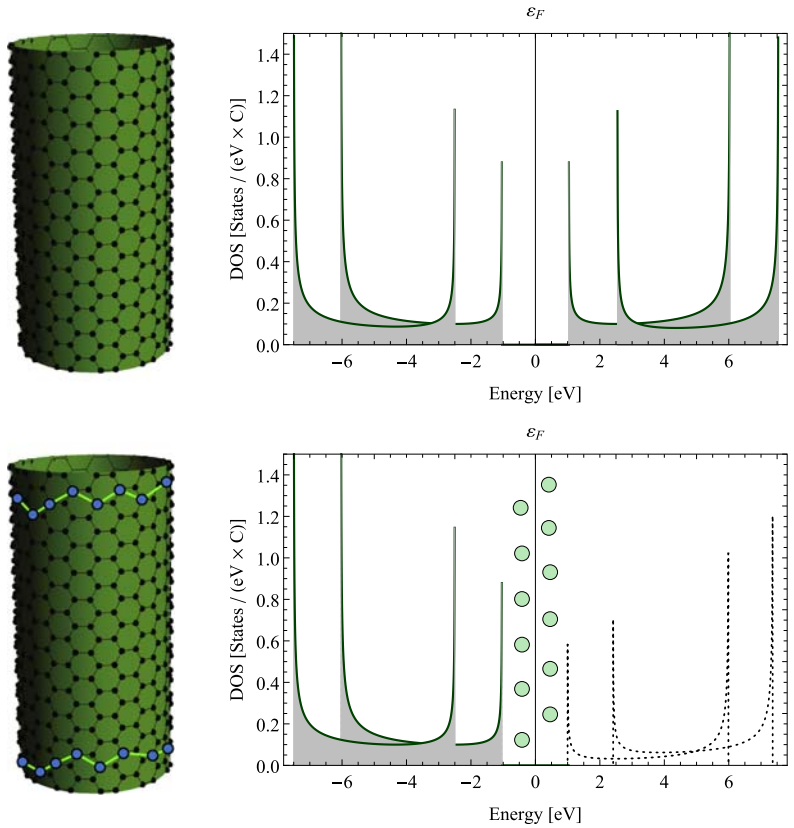

Figure 2.10

Plots of the electronic density of states versus energy for an ideally pristine (upper part) and a defected semiconducting SWCNT (lower part), computed using the tight-binding model. The electronic states of the defects forming the effective SWCNT edges are given in *green circles*. They are distributed around Fermi level at zero energy above which the DOS perishes gradually as the energy goes higher.

single walled carbon nanotubes exploited for molecular electronics and spintronics. The transport properties of these novel multifunctional materials have been reviewed in this chapter in the light of noninvasive spectroscopic techniques which involve: RS, IRR, and ESR. Through brief introductions made at the beginning of each section, these three contactless spectroscopic tools have been described in detail.

Acknowledgments

The authors greatly acknowledge funding provided by the Institute of Physics Belgrade, through the grant by the Ministry of Education, Science, and Technological Development of the Republic of Serbia.

References

[1] D.M. Djokić, B. Stojadinović, D. Stepanenko, Z. Dohčević-Mitrović, Probing charge carrier transport regimes in $BiFeO^3$ nanoparticles by Raman spectroscopy, Scripta Mater. 181 (2020) 6−9, https://doi.org/10.1016/j.scriptamat.2020.02.008.

[2] M. Radović, Z. Dohčević-Mitrović, N. Paunović, S. Bošković, N. Tomić, N. Tadić, I. Belča, Infrared study of plasmon-phonon coupling in pure and Nd-doped CeO^{2-y} nanocrystals, J. Phys. D Appl. Phys. 48 (2015) 065301−065306, https://doi.org/10.1088/0022-3727/48/6/065301.

[3] W.D. Rice, R.T. Weber, P. Nikolaev, S. Arepalli, V. Berka, A.L. Tsai, J. Kono, Spin relaxation times of single-wall carbon nanotubes, Phys. Rev. B 88 (2013) 041401−041405, https://doi.org/10.1103/PhysRevB.88.041401.

[4] S.S. Mitra, Infrared and Raman Spectra Due to Lattice Vibrations, Springer US, 1969, pp. 333−451, https://doi.org/10.1007/978-1-4757-1123-3_14.

[5] M. Cardona, Light Scattering in Solids I - Introductory Concepts, Springer-Verlag, Berlin), 1983.

[6] L.A. Falkovsky, Investigation of semiconductors with defects using Raman scattering, Phys. Usp. 47 (2004) 249−272, https://doi.org/10.1070/pu2004v047n03abeh001735.

[7] L.A. Falkovsky, Raman scattering of light by electrons in a metal with impurities, Sov. Phys. JETP 68 (1989) 661−663.

[8] A. Zawadowski, M. Cardona, Theory of Raman scattering on normal metals with impurities, Phys. Rev. B 42 (1990) 10732−10734, https://doi.org/10.1103/PhysRevB.42.10732.

[9] T.P. Devereaux, Theory for the effects of impurities on the Raman spectra of superconductors, Phys. Rev. B 45 (1992) 12965−12975, https://doi.org/10.1103/PhysRevB.45.12965.

[10] E.Y. Sherman, O.V. Misochko, Raman scattering in metals with disorder: beyond the zero-momentum approximation, J. Phys. Condens. Matter 15 (2003) 3751−3758, https://doi.org/10.1088/0953-8984/15/22/309.

[11] T.P. Devereaux, R. Hackl, Inelastic light scattering from correlated electrons, Rev. Mod. Phys. 79 (2007) 175−233, https://doi.org/10.1103/RevModPhys.79.175.

[12] A.A. Abrikosov, L.P. Gorkov, I.E. Dzyaloshinsky, Quantum Field Theoretical Methods in Statistical Physics, Pergamon Press, Oxford), 1965.

[13] H. Zhang, K. Kajiyoshi, Hydrothermal synthesis and size-dependent properties of multiferroic bismuth ferrite crystallites, J. Am. Ceram. Soc. 93 (2010) 3842, https://doi.org/10.1111/j.1551-2916.2010.03953.x.

[14] F. Kubel, H. Schmid, Structure of a ferroelectric and ferroelastic monodomain crystal of the perovskite $BiFeO_3$, Acta Crystallogr. B 46 (1990) 698, https://doi.org/10.1107/S0108768190006887.

[15] J.-G. Park, M.D. Le, J. Jeong, S. Lee, Structure and spin dynamics of multiferroic $BiFeO^3$, J. Phys. Condens. Mat. 26 (2014) 433202, https://doi.org/10.1088/0953-8984/26/43/433202.

[16] G. Catalan, J.F. Scott, Physics and applications of bismuth ferrite, Adv. Mater. 21 (2009) 2463−2485, https://doi.org/10.1002/adma.200802849.

[17] C.-H. Yang, D. Kan, I. Takeuchi, V. Nagarajan, J. Seidel, Doping $BiFeO^3$: approaches and enhanced functionality, Phys. Chem. Chem. Phys. 14 (2012) 15953, https://doi.org/10.1039/C2CP43082G.

[18] J.D. Bucci, B.K. Robertson, W.J. James, The precision determination of the lattice parameters and the coefficients of thermal expansion of $BiFeO_3$, J. Appl. Cryst. 5 (1972) 187−191, https://doi.org/10.1107/S0021889872009173.

[19] J.F. Ihlefeld, N.J. Podraza, Z.K. Liu, R.C. Rai, X. Xu, T. Heeg, Y.B. Chen, J. Li, R.W. Collins, J.L. Musfeldt, X.Q. Pan, J. Schubert, R. Ramesh, D.G. Schlom, Optical band gap of $BiFeO^3$ grown by molecular-beam epitaxy, Appl. Phys. Lett. 92 (2008) 142908, https://doi.org/10.1063/1.2901160.

[20] Y. Xu, M. Shen, Structure and optical properties of nanocrystalline $BiFeO^3$ films prepared by chemical solution deposition, Mater. Lett. 62 (2008) 3600, https://doi.org/10.1016/j.matlet.2008.04.006.

[21] A. Kumar, R.C. Rai, N.J. Podraza, S. Denev, M. Ramirez, Y.-H. Chu, L.W. Martin, J. Ihlefeld, T. Heeg, J. Schubert, D.G. Schlom, J. Orenstein, R. Ramesh, R.W. Collins, J.L. Musfeldt, V. Gopalan, Linear and nonlinear optical properties of $BiFeO_3$, Appl. Phys. Lett. 92 (2008) 121915, https://doi.org/10.1063/1.2901168.
[22] J. Allibe, K. Bougot-Robin, E. Jacquet, I.C. Infante, S. Fusil, C. Carrétéro, J.-L. Reverchon, B. Marcilhac, D. Creté, J.-C. Mage, A. Barthélémy, M. Bibes, Optical properties of integrated multiferroic $BiFeO^3$ thin films for microwave applications, Appl. Phys. Lett. 96 (2010) 182902, https://doi.org/10.1063/1.3402763.
[23] M. Shariq, D. Kaur, V.S. Chandel, M.A. Siddiqui, Investigation on multiferroic properties of $BiFeO^3$ ceramics, Mater. Sci. Poland 31 (2013) 471, https://doi.org/10.2478/s13536-013-0128-2.
[24] S.J. Clark, J. Robertson, Band gap and Schottky barrier heights of multiferroic $BiFeO_3$, Appl. Phys. Lett. 90 (2007) 132903, https://doi.org/10.1063/1.2716868.
[25] H. Wang, Y. Zheng, M.-Q. Cai, H. Huang, H.L. Chan, First-principles study on the electronic and optical properties of $BiFeO_3$, Solid State Commun. 149 (2009) 641, https://doi.org/10.1016/j.ssc.2009.01.023.
[26] S.R. Basu, L.W. Martin, Y.H. Chu, M. Gajek, R. Ramesh, R.C. Rai, X. Xu, J.L. Musfeldt, Photoconductivity in $BiFeO^3$ thin films, Appl. Phys. Lett. 92 (2008) 091905, https://doi.org/10.1063/1.2887908.
[27] A. Mukherjee, M. Banerjee, S. Basu, N.T.K. Thanh, L.A.W. Green, M. Pal, Enhanced magnetic and electrical properties of Y and Mn co-doped $BiFeO^3$ nanoparticles, Physica B: Cond. Matt. 448 (2014) 199−203, https://doi.org/10.1016/j.physb.2014.03.082.
[28] S. Ruby, S.S.R. Inbanathan, Structural properties and electrical conduction mechanisms of $Bi^{0.9}Sm^{0.05}Tb^{0.05}FeO^3$ thin film, Appl. Surf. Sci. 449 (2018) 10−14, https://doi.org/10.1016/j.apsusc.2017.11.231.
[29] H. Fukumura, H. Harima, K. Kisoda, M. Tamada, Y. Noguchi, M. Miyayama, Raman scattering study of multiferroic $BiFeO^3$ single crystal, J. Magn. Magn. Mat. 310 (2007) e367−e369, https://doi.org/10.1016/j.jmmm.2006.10.282.
[30] J. Hlinka, J. Pokorny, S. Karimi, I.M. Reaney, Angular dispersion of oblique phonon modes in $BiFeO^3$ from micro-Raman scattering, Phys. Rev. B 83 (2011) 020101−020104, https://doi.org/10.1103/PhysRevB.83.020101.
[31] J. Bielecki, P. Svedlindh, D.T. Tibebu, S. Cai, S.-G. Eriksson, L. Börjesson, C.S. Knee, Structural and magnetic properties of isovalently substituted multiferroic $BiFeO^3$: insights from Raman spectroscopy, Phys. Rev. B 86 (2012) 184422−184437, https://doi.org/10.1103/PhysRevB.86.184422.
[32] D.L. Rousseau, R.P. Bauman, S.P.S. Porto, Normal mode determination in crystals, J. Raman Spectrosc. 10 (1981) 253−290, https://doi.org/10.1002/jrs.1250100152.
[33] A. Otto, J. Timper, J. Billmann, G. Kovacs, I. Pockrand, Surface roughness induced electronic Raman scattering, Surf. Sci. 92 (1980) L55−L57, https://doi.org/10.1016/0039-6028(80)90237-X.
[34] R. Monreal, F. Flores, Y. Gao, T. López-Ríos, Raman scattering by electron-hole pairs at metal surfaces, Europhys. Lett. 4 (1987) 115−120, https://doi.org/10.1209/0295-5075/4/1/019.
[35] C.Y. Chen, E. Burstein, S. Lundquist, Giant Raman scattering by pyridine and cn adsorbed on silver, Solid State Commun. 32 (1979) 63−66, https://doi.org/10.1016/0038-1098(79)90998-0.
[36] H.L. Liu, S. Yoon, S.L. Cooper, S.-W. Cheong, P.D. Han, D.A. Payne, Probing anisotropic magnetotransport in manganese perovskites using Raman spectroscopy, Phys. Rev. B 58 (1998) R10115−R10118, https://doi.org/10.1103/PhysRevB.58.R10115.
[37] N.F. Mott, E.A. Davis, Electronic Processes in Non-crystalline Materials, Oxford University Press, 1979.
[38] A.L. Efros, B.I. Shklovskii, Coulomb gap and low temperature conductivity of disordered systems, J. Phys. C Solid State Phys. 8 (1975) L49−L51, https://doi.org/10.1088/0022-3719/8/4/003.
[39] N.V. Arginskaya, V.I. Kozub, Potential influence of pre-exponential factors on the temperature dependence of variable-range hopping conductivity, Soviet JETP 79 (1994) 466−472.
[40] A. Aharony, Y. Zhang, M.P. Sarachik, Universal crossover in variable range hopping with Coulomb interactions, Phys. Rev. Lett. 68 (1992) 3900−3903, https://doi.org/10.1103/PhysRevLett.68.3900.

[41] L. Zuppiroli, L. Forró, Hopping conductivity in polaronic situations, Phys. Lett. A 141 (1989) 181−185, https://doi.org/10.1016/0375-9601(89)90785-8.
[42] B. Stojadinović, Faculty of Physics, University of Belgrade, 2018 (Ph.D. thesis).
[43] O. Gunnarsson, M. Calandra, J.E. Han, *Colloquium*: saturation of electrical resistivity, Rev. Mod. Phys. 75 (2003) 1085−1099, https://doi.org/10.1103/RevModPhys.75.1085.
[44] N.E. Hussey, K. Takenaka, H. Takagi, Universality of the Mott-Ioffe-Regel limit in metals, Philos. Mag. A 84 (2004) 2847−2864, https://doi.org/10.1080/14786430410001716944.
[45] A. Ioffe, A. Regel, Non-crystalline, amorphous and liquid electronic semiconductors, Prog. Semicond. 4 (1960) 237−291.
[46] N.F. Mott, Conduction in non-crystalline systems IX. The minimum metallic conductivity, Philos. Mag. J. Theor. Exp. Appl. Phys 26 (4) (1972) 1015−1026, https://doi.org/10.1080/14786437208226973.
[47] F. Gervais, Infrared dispersion in several polar-mode crystals, Opt. Commun. 22 (1977) 116−118, https://doi.org/10.1016/0030-4018(77)90260-7.
[48] F. Gervais, Optical conductivity of oxides, Mater. Sci. Eng. R Rep. 39 (2002) 29−92, https://doi.org/10.1016/S0927-796X(02)00073-6.
[49] R.F. Wallis, M. Balkanski, Many-body Aspects of Solid State Spectroscopy, Elsevier Science Ltd, Amsterdam, the Netherlands, 1986.
[50] A.A. Kukharskii, Plasmon-phonon coupling in GaAs, Solid State Commun. 13 (1973) 1761−1765, https://doi.org/10.1016/0038-1098(73)90724-2.
[51] D.A.G. Bruggeman, Berechnung verschiedener physikalischer Konstanten von heterogenen substanzen. I. Dielektrizitatskonstanten und Leitfahigkeiten der Mischkorper aus isotropen Substanzen, Ann. Phys. 416 (7) (1935) 636−664, https://doi.org/10.1002/andp.19354160705.
[52] Z.V. Popović, M. Grujić-Brojčin, N. Paunović, M.M. Radonjić, V.D. Araújo, M.I.B. Bernardi, M.M. de Lima, A. Cantarero, Far-infrared spectroscopic study of CeO^2 nanocrystals, J. Nanopart. Res. 17 (2015) 23−30, https://doi.org/10.1007/s11051-015-2859-y.
[53] A. Younis, D. Chu, S. Li, Cerium oxide nanostructures and their applications, in: Functionalized Nanomaterials, 2016, pp. 52−68, https://doi.org/10.5772/65937. Ch. 3.
[54] P. Jasinski, T. Suzuki, H.U. Anderson, Nanocrystalline undoped ceria oxygen sensor, Sensor. Actuator. B Chem. 95 (2003) 73−77, https://doi.org/10.1016/S0925-4005(03)00407-6.
[55] X. Han, J. Lee, H.-I. Yoo, Oxygen-vacancy-induced ferromagnetism in CeO^2 from first principles, Phys. Rev. B 79 (2009) 100403−100406, https://doi.org/10.1103/PhysRevB.79.100403.
[56] G. Feher, A.F. Kip, Electron spin resonance absorption in metals. I Experimental, Phys. Rev. 98 (1955) 337−348, https://doi.org/10.1103/PhysRev.98.337.
[57] F.J. Dyson, Electron spin resonance absorption in metals. II. Theory of electron diffusion and the skin effect, Phys. Rev. 98 (1955) 349−359, https://doi.org/10.1103/PhysRev.98.349.
[58] M.I. Azbel, V.I. Gerasimenko, I.M. Lifshitz, Paramagnetic resonance and polarization of nuclei in metals, Sov. Phys. JETP 5 (1957) 986−996.
[59] M.I. Azbel, V.I. Gerasimenko, I.M. Lifshitz, On the theory of paramagnetic resonance in metals, Sov. Phys. JETP 8 (1959) 480−487.
[60] D.M. Djokić, D. Stepanenko, Z. Dohčević-Mitrović, Extreme conduction electron spin resonance: $A/B \rightarrow^{(5+3\sqrt{3})/4}$, the universal limit of lineshape asymmetry ratio, J. Magn. Magn. Mater. 491 (2019) 165616, https://doi.org/10.1016/j.jmmm.2019.165616.
[61] A.C. Chapman, P. Rhodes, E.F.W. Seymour, The effect of eddy currents on nuclear magnetic resonance in metals, Proc. Phys. Soc. B 70 (1957) 345−360, https://doi.org/10.1088/0370-1301/70/4/301.
[62] P.M. Platzman, P.A. Wolff, Spin-wave excitation in nonferromagnetic metals, Phys. Rev. Lett. 18 (1967) 280−283, https://doi.org/10.1103/PhysRevLett.18.280.
[63] H.R. Webb, Electron-spin-resonance line shape in spherical metal particles, Phys. Rev. 158 (1967) 225−233, https://doi.org/10.1103/PhysRev.158.225.
[64] J.H. Pifer, R. Magno, Conduction-electron spin resonance in a lithium film, Phys. Rev. B 3 (1971) 663−673, https://doi.org/10.1103/PhysRevB.3.663.

[65] A.H. Kahn, Theory of microwave eddy currents and paramagnetic resonance in materials of intermediate conductivity, Phys. Rev. B 16 (1977) 64–72, https://doi.org/10.1103/PhysRevB.16.64.
[66] J.I. Kaplan, J. Reuben, Electron spin resonance line shapes of paramagnetic species on surfaces, J. Phys. Chem. 86 (1982) 4465–4466, https://doi.org/10.1021/j100220a001.
[67] A.G. Marshall, D.C. Roe, Dispersion versus absorption: spectral line shape analysis for radiofrequency and microwave spectrometry, Analyt. Chem. 50 (1978) 756–763, https://doi.org/10.1021/ac50027a023.
[68] L. Walmsley, G. Ceotto, J.H. Castilho, C. Rettori, Magnetic field modulation frequency, sample size and electromagnetic configuration effects on the spin resonance spectra of graphite intercalation compounds, Synth. Met. 30 (1989) 97–107, https://doi.org/10.1016/0379-6779(89)90645-0.
[69] L. Walmsley, Translating conduction-electron spin-resonance lines into lorentzian lines, J. Magn. Reson. A 122 (1996) 209–213, https://doi.org/10.1006/jmra.1996.0196.
[70] M. Oshikawa, I. Affleck, Electron spin resonance in S=½ antiferromagnetic chains, Phys. Rev. B 65 (2002) 134410–134437, https://doi.org/10.1103/PhysRevB.65.134410.
[71] J.P. Joshi, S.V. Bhat, On the analysis of broad Dysonian electron paramagnetic resonance spectra, J. Magn. Res. 168 (2004) 284–287, https://doi.org/10.1016/j.jmr.2004.03.018.
[72] K.W. Blazey, K.A. Müller, F. Blatter, E. Schumacher, Conduction electron spin resonance of Caesium metallic clusters in zeolite X, Europhys. Lett. 4 (1987) 857–861, https://doi.org/10.1209/0295-5075/4/7/017.
[73] J.J. van der Klink, H.B. Brom, NMR in metals, metal particles and metal cluster compounds, Prog. Nucl. Magn. Reson. Spectr. 36 (2) (2000) 89–201, https://doi.org/10.1016/S0079-6565(99)00020-5.
[74] S. Iijima, Helical microtubules of graphitic carbon, Nature 354 (1991) 56–58, https://doi.org/10.1038/354056a0.
[75] L. Forró, C. Schönenberger, Physical Properties of Multi-Wall Nanotubes, Springer Berlin Heidelberg, Berlin, Heidelberg, 2001, pp. 329–391, https://doi.org/10.1007/3-540-39947-X_13.
[76] D.M. Djokić, A. Goswami, Quantum yield in polymer wrapped single walled carbon nanotubes: a computational model, Nanotechnology 28 (2017) 465204, https://doi.org/10.1088/1361-6528/aa8f38.
[77] A. Bachtold, M. Henny, C. Terrier, C. Strunk, C. Schönenberger, J.-P. Salvetat, J.-M. Bonard, L. Forró, Contacting carbon nanotubes selectively with low-ohmic contacts for four-probe electric measurements, Appl. Phys. Lett. 73 (1998) 274–276, https://doi.org/10.1063/1.121778.
[78] A. Bachtold, C. Strunk, J.-P. Salvetat, J.-M. Bonard, L. Forró, T. Nussbaumer, C. Schönenberger, Aharonov-Bohm oscillations in carbon nanotubes, Nature 397 (1999) 673–675, https://doi.org/10.1038/17755.
[79] L. Langer, V. Bayot, E. Grivei, J.-P. Issi, J.P. Heremans, C.H. Olk, L. Stockman, C. Van Haesendonck, Y. Bruynseraede, Quantum transport in a multiwalled carbon nanotube, Phys. Rev. Lett. 76 (1996) 479–482, https://doi.org/10.1103/PhysRevLett.76.479.
[80] W. Yi, L. Lu, Z. Dian-lin, Z.W. Pan, S.S. Xie, Linear specific heat of carbon nanotubes, Phys. Rev. B 59 (1999) R9015–R9018, https://doi.org/10.1103/PhysRevB.59.R9015.
[81] M. Bockrath, D.H. Cobden, J. Lu, A.G. Rinzler, R.E. Smalley, L. Balents, P.L. McEuen, Luttinger-liquid behaviour in carbon nanotubes, Nature 998 (1999) 598–601, https://doi.org/10.1038/17569.